Inorganic Chemistry

Article

Underlying Spin–Orbit Coupling Structure of Intervalence Charge Transfer Bands in Dinuclear Polypyridyl Complexes of Ruthenium and Osmium

Deanna M. D'Alessandro,[†] Peter H. Dinolfo,[‡] Murray S. Davies,[†] Joseph T. Hupp,[‡] and F. Richard Keene*,[†]

School of Pharmacy and Molecular Sciences, James Cook University, Townsville, Queensland 4811, Australia, and Department of Chemistry, Northwestern University, 211 Sheridan Road, Evanston, IL 60208-3113

The mixed-valence systems *meso*- and *rac*-[{M(bpy)$_2$}$_2$(μ-BL)]$^{5+}$ {M = Ru, Os; BL = a series of polypyridyl bridging ligands such as 2,3-bis(2-pyridyl)benzoquinoxaline (dpb)} are characterized by multiple intervalence charge transfer (IVCT) and interconfigurational (IC) bands in the mid-infrared and near-infrared (NIR) regions. Differences in the relative energies of the IC transitions for the fully oxidized (+6) states of the osmium systems demonstrate that stereochemical effects lead to fundamental changes in the energy levels of the metal-based dπ orbitals, which are split by spin–orbit coupling and ligand-field asymmetry. An increase in the separation between the IC bands as BL is varied reflects the increase in the degree of electronic coupling through the series of ruthenium and osmium complexes. The increase in the IVCT bandwidths for the former is therefore attributed to the increase in the separation of the three underlying components of the bands. Stark effect measurements reveal small dipole moment changes accompanying IVCT excitation in support of the localized-to-delocalized or delocalized classification for the dinuclear ruthenium and osmium systems.

Introduction

The intervalence charge transfer (IVCT)[1] transitions generated by dinuclear mixed-valence complexes provide one of the most sensitive and powerful probes to elucidate the factors that govern activation barriers to intramolecular electron transfer. According to the classical formalism pioneered by Hush,[2,3] the energy (ν_{max}) of the IVCT bands may be expressed in terms eq 1,

$$\nu_{max} = \lambda_i + \lambda_o + \Delta E_0 + \Delta E' \tag{1}$$

where the Franck–Condon factors, λ_i and λ_o, correspond to the reorganizational energies within the inner- and outer-sphere (respectively); the redox asymmetry, ΔE_0, is the difference in energy between vibrationally relaxed initial and final states in the hypothetical absence of electronic coupling; and $\Delta E'$ reflects any additional energy contributions due to spin–orbit coupling and ligand-field asymmetry.

A pivotal problem in the analysis of mixed-valence complexes is the extent of electronic delocalization between the metal centers, which depends on the relative values of the sum of the factors on the right-hand side of eq 1 and $2H_{ab}$ (where H_{ab} is the magnitude of the electronic coupling): this sum exceeds $2H_{ab}$ in localized (Class II[4]) systems, whereas it is less than or equal to $2H_{ab}$ in the delocalized (Class III[4]) case. While clear examples of localized (Class II) and delocalized (Class III) systems have been reported in several comprehensive surveys of dinuclear mixed-valence complexes,[5–13] a number of recent reviews have highlighted

* To whom correspondence should be addressed. E-mail: Richard.Keene@jcu.edu.au. Fax: +61-(0)7-4781-6078.

† James Cook University.

‡ Northwestern University.

(1) We are using "intervalence charge transfer" and its acronym IVCT loosely—as is the practice in this area—to mean any intervalence-derived transition, even if charge-transfer character is minor.

(2) Hush, N. S. *Progr. Inorg. Chem.* **1967**, *8*, 391–444.

(3) Hush, N. S. *Electrochim. Acta* **1968**, *13*, 1005–1023.

(4) Robin, M. B.; Day, P. *Adv. Inorg. Chem. Radiochem.* **1967**, *10*, 247–403.

(5) Hush, N. S. *Coord. Chem. Rev.* **1985**, *64*, 135–157.

(6) Creutz, C. *Prog. Inorg. Chem.* **1983**, *30*, 1–73.

(7) Crutchley, R. J. *Adv. Inorg. Chem.* **1994**, *41*, 273–325.

(8) Kalyanasundaram, K.; Nazeeruddin, M. K. *Inorg. Chim. Acta* **1994**, *226*, 213–230.

(9) Ward, M. D. *Chem. Soc. Rev.* **1995**, *24*, 121–134.

systems which exhibit intermediate behavior in the "Class II−III" regime.[14−16] In reality, the transitions between the classes are not abrupt, and their distinction is based on the relative time-scales of the solvent, vibrational, and electronic motions.[14]

H_{ab} is typically evaluated from eq 2,[17,18] where r_{ab} is the diabatic charge-transfer distance, e is the unit electronic charge, and $|\mu_{12}|$ is the adiabatic transition moment which may be calculated from the integrated intensity of the absorption band.

$$H_{ab} = \frac{|\mu_{12}|}{er_{ab}}\nu_{max} \qquad (2)$$

The determination of the "class" of a mixed-valence system based on this criterion is often complicated by the inability to accurately determine H_{ab}. While r_{ab} is typically equated with the through-space geometrical distance between the metal centers, the *effective* charge-transfer distance may be shorter due to electronic delocalization, self-polarization, and other effects[19−23] so that eq 2 provides a lower limit only for H_{ab}.[14] Electroabsorption (Stark effect) measurements provide a means of measurement of *effective* charge-transfer distances.[21]

In addition to electronic delocalization effects, band-shape analyses are frequently complicated by the presence of multiple overlapping IVCT and interconfigurational (IC) transitions. These arise from the effects of spin−orbit coupling and ligand-field asymmetry at low-spin $M^{III}(d\pi^5)$ centers (M = Fe, Ru, Os), where the t_{2g} orbitals are split into three $d\pi$ levels (Kramer's doublets) which are linear combinations of the d_{xy}, d_{xz}, and d_{yz} atomic orbitals.[14,24−27] The compositions and energy splittings between the levels are governed by the magnitude of the spin−orbit coupling constant of the metal and the electronic character of the surrounding ligands. Three IVCT transitions are expected due to excitation from each of the $M^{II}(d\pi)$ orbitals to the
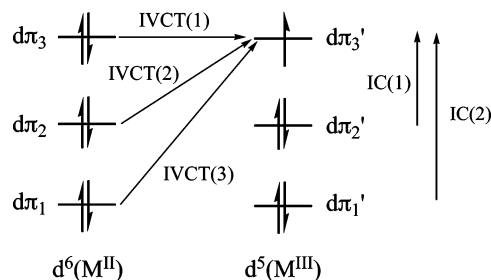
(10) Barbara, P. F.; Meyer, T. J.; Ratner, M. A. *J. Phys. Chem.* **1996**, *100*, 13148−13168.
(11) Launay, J.-P. *Chem. Soc. Rev.* **2001**, *30*, 386-397.
(12) Kaim, W.; Klein, A.; Glöckle, M. *Acc. Chem. Res.* **2000**, *33*, 755−763.
(13) Chen, P.; Meyer, T. J. *Chem. Rev.* **1998**, *98*, 1439−1477.
(14) Demadis, K. D.; Hartshorn, C. M.; Meyer, T. J. *Chem. Rev.* **2001**, *101*, 2655−2685.
(15) Nelsen, S. F. *Chem. Eur. J.* **2000**, *6*, 581−588.
(16) Brunschwig, B. S.; Creutz, C.; Sutin, N. *Chem. Soc. Rev.* **2002**, *31*, 168−184.
(17) Creutz, C.; Newton, M. D.; Sutin, N. *J. Photochem.* **1994**, *82*, 47−59.
(18) Cave, R. J.; Newton, M. D. *Chem. Phys. Lett.* **1996**, *249*, 15−19.
(19) Bublitz, G. U.; Boxer, S. G. *Annu. Rev. Phys. Chem.* **1997**, *48*, 213−242.
(20) Brunschwig, B. S.; Creutz, C.; Sutin, N. *Coord. Chem. Rev.* **1998**, *177*, 61−79.
(21) Walters, K. A. *Compr. Coord. Chem. II* **2003**, *2*, 303−313.
(22) Ferretti, A. *Coord. Chem. Rev.* **2003**, *238−239*, 127−141.
(23) Vance, F. W.; Williams, R. D.; Hupp, J. T. *Int. Rev. Phys. Chem.* **1998**, *17*, 307−329.
(24) Kober, E. M.; Meyer, T. J. *Inorg. Chem.* **1982**, *21*, 3967−3977.
(25) Kober, E. M.; Goldsby, K. A.; Narayana, D. N. S.; Meyer, T. J. *J. Am. Chem. Soc.* **1983**, *105*, 4303−4309.
(26) Kober, E. M.; Meyer, T. J. *Inorg. Chem.* **1983**, *22*, 1614−1616.
(27) Neyhart, G., Ph.D. Thesis, University of North Carolina at Chapel Hill, 1988.

Figure 1. Schematic illustrations of the IVCT and IC transitions in a mixed-valence dinuclear complex, $[M^{II}M^{III}]$.

hole at M^{III}, in addition to two $d\pi \rightarrow d\pi$ IC transitions between the Kramer's doublets, as shown in Figure 1.

Meyer and co-workers[14,25] have proposed semiquantitative relationships between the energies of the IC and IVCT bands in weakly coupled Class II systems. The energy splittings $\Delta E_{so(1)}$ and $\Delta E_{so(2)}$ represent the $\Delta E'$ contribution to the intramolecular electron-transfer barrier in eq 1.

$$\Delta E_{so(1)} \approx \nu_{max}\{IVCT(2)\} - \nu_{max}\{IVCT(1)\}$$

$$\Delta E_{so(2)} \approx \nu_{max}\{IVCT(3)\} - \nu_{max}\{IVCT(1)\} \qquad (3)$$

The recognition of the existence of IVCT spectral components and knowledge of their relative intensities is crucial for the accurate analysis of IVCT bands. The parameters λ_i, λ_o, and H_{ab} may differ for the three transitions, and the lowest-energy transition, IVCT(1), corresponds directly to the thermal electron-transfer pathway. It must be noted that while spin−orbit coupling effects are expected to be dominant for Os complexes (the spin−orbit coupling constant for Os is $\xi_{Os} \approx 3000$ cm^{-1}) other contributions from electronic coupling and ligand-field effects are important and will be dominant for Ru and Fe complexes (where $\xi_{Ru} \approx 1000$ cm^{-1} and $\xi_{Fe} \approx 800$ cm^{-1}).

The complexity of factors which influence intramolecular electron transfer, as well as their sensitivity to the properties of the environment, underlie the need for *systematic* experimental studies to probe the factors which govern the transition between the localized and delocalized regimes. To date, these factors have been investigated by varying the "global" features of dinuclear complexes such as the identity and coordination environments of their constituent metal centers or through the introduction of redox asymmetry. The reorganizational energy contributions have typically been assessed by varying the macroscopic features of the external environment such as the solvent, anions, and temperature.

In recent work from our laboratory, comparisons between the characteristics of the IVCT transitions generated by the diastereoisomers *meso*- and *rac*-$[\{M(bpy)_2\}_2(\mu\text{-BL})]^{5+}$ (M = Ru, Os; and BL represents the polypyridyl bridging ligands shown in Figure 2) have provided detailed insights into the contributions of redox asymmetry to the electron-transfer barrier due to stereochemically directed structural distortions[28] and ion-pairing interactions,[29] as well as the outer-sphere reorganizational contributions due to spatially directed solvent interactions.[30] While the electrochemical, spectral, and photophysical properties of complexes of this genre have
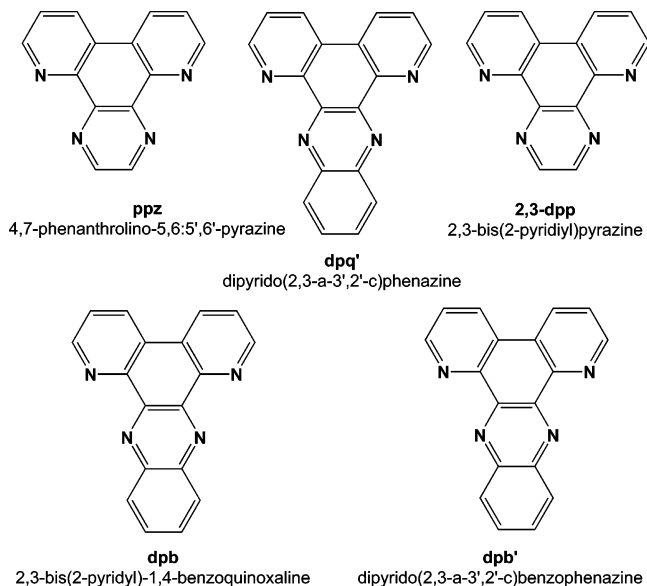
Figure 2. Polypyridyl bridging ligands employed in the present study.

been the subject of extensive research efforts over the past two decades,[31-35] these earlier measurements were conducted without regard for the *inherent* stereoisomeric complexities which are now known to influence their IVCT characteristics.[28-30,36] The comparison of the IVCT characteristics of diastereoisomers presents several attractive features: the identity and coordination environments of the component metal centers are maintained, the complexes are structurally rigid, and the dimensions of the clefts may be varied in a subtle and systematic way through stereochemical variation, bridging ligand modification, or the judicious positioning of substituents on the terminal polypyridyl ligands.

The present work extends our investigations into the use of stereoisomers as novel probes for the factors that govern the electron-transfer barrier[29] through the examination of the underlying contribution of spin−orbit coupling and ligand-field asymmetry to the IVCT line-shape ($\Delta E'$ in eq 1) in dinuclear ruthenium and osmium complexes. Stark effect spectroscopy on the meso diastereoisomers of the series of complexes provides measures of the dipole moment changes accompanying IVCT excitation.

The elucidation of these fundamental contributions to the IVCT bands has important implications for the understanding of spatial influences on electron migration in natural processes such as photosynthesis and ultimately for exploiting stereochemical effects in artificial materials capable of performing useful light- and redox-induced functions.

Experimental Section

Materials. 2,3-Bis(2-pyridyl)pyrazine (2,3-dpp; Aldrich, 98%), stannous chloride ($SnCl_2 \cdot 2H_2O$, Ajax), potassium hexafluorophosphate (KPF_6; Aldrich, 98%), zinc chloride ($ZnCl_2.xH_2O$; Fluka, 98%), nitrosonium hexafluorophosphate ($NOPF_6$ stored under Ar; Alfa Aesar, 96%), sodium toluene-4-sulfonate (Aldrich, 98%), DOWEX 1 × 8, 50−100 mesh (Aldrich) anion-exchange resin, *n*-butyronitrile (Aldrich, 99+%), 2,2,2-trifluoroethanol (Aldrich, 98%), and laboratory reagent solvents were used as received.

Prior to use, tetra-*n*-butylammonium hexafluorophosphate ([(*n*-$C_4H_9)_4N]PF_6$; Fluka, 99+%) was dried in vacuo at 60 °C, acetonitrile (CH_3CN; Aldrich, 99.9+%) was distilled over CaH_2, and ferrocene (Fc; BDH) was purified by sublimation.

SP Sephadex C-25 (Amersham Pharmacia Biotech) was employed for the chromatographic separation of complexes.[37]

General. 1D and 2D ^{1}H NMR spectra were collected on a Varian Mercury 300 MHz spectrometer. ^{1}H NMR chemical shifts for all complexes are reported relative to 99.9% d_3-acetonitrile {CD_3CN; Cambridge Isotope Laboratories (CIL)} at $\delta = 1.93$ ppm. ^{1}H NMR assignments were performed with the assistance of COSY experiments to identify each pyridine ring system. Elemental microanalyses were performed at the Microanalytical Unit in the Research School of Chemistry, Australian National University.

Electrochemistry. Electrochemical measurements were performed under argon using a Bioanalytical Systems (BAS) 100A electrochemical analyzer. Cyclic (CV) and differential pulse (DPV) voltammograms were recorded in a standard three-electrode cell using a glassy carbon or platinum button working electrode, a platinum wire auxiliary electrode, and an Ag/AgCl reference electrode (0.1 M [(*n*-$C_4H_9)_4N]PF_6$ in CH_3CN). Ferrocene was added as an internal standard on completion of each experiment {the ferrocene/ferrocenium couple (Fc^+/Fc^0) occurred at +550 mV versus Ag/AgCl}. Solutions contained 0.1 M [(*n*-$C_4H_9)_4N]PF_6$ as electrolyte. Cyclic voltammetry was performed with a sweep rate of 100 mV s^{-1}; differential pulse voltammetry was conducted with a sweep rate of 4 mV s^{-1} and a pulse amplitude, width, and period of 50 mV, 60 ms, and 1 s, respectively. All potentials are reported ±3 mV.

UV/Vis/NIR Spectroelectrochemistry. UV/vis/NIR spectroelectrochemistry was performed using a CARY 5E spectrophotometer interfaced to Varian WinUV software. The absorption spectra of the electrogenerated mixed-valence species were obtained in situ by the use of a cryostatted optically semi-transparent thin-layer electrosynthetic (OSTLE) cell.[38] An account of the procedure employed in the spectroelectrochemical measurements has been detailed previously.[36] Solutions for the spectroelectrochemial experiments contained 0.1 M [(*n*-$C_4H_9)_4N]PF_6$ supporting electrolyte in CH_3CN and the complex (ca. 1 × 10^{-3} M).

The analysis and spectral deconvolution of the data were performed as described in a previous report.[29] The IVCT spectra were scaled as $\int \epsilon(\nu)/\nu \ d\nu$,[2,39] and deconvolution of the NIR transitions was performed using the curve-fitting subroutine implemented within the GRAMS32 commercial software package, as described previously.[36] On the basis of the reproducibility of the parameters obtained from the deconvolutions, the uncertainties in

(28) D'Alessandro, D. M.; Kelso, L. S.; Keene, F. R. *Inorg. Chem.* **2001**, *40*, 6841−6844.

(29) D'Alessandro, D. M.; Junk, P. C.; Keene, F. R. *Supramol. Chem.* **2005**, *17*, 529−542.

(30) D'Alessandro, D. M.; Keene, F. R. *Chem. Phys.* **2006**, DOI: 10.016/j.chemphys.2005.09.016.

(31) Garcia, C. G.; de Lima, J. F.; Iha, N. Y. M. *Coord. Chem. Rev.* **2000**, *196*, 219−247.

(32) Belser, P.; Bernhard, S.; Blum, C.; Beyeler, A.; De Cola, L.; Balzani, V. *Coord. Chem. Rev.* **1999**, *190*, 0−192; 155−169.

(33) Balzani, V.; Juris, A.; Venturi, M.; Campagna, S.; Serroni, S. *Chem. Rev.* **1996**, *96*, 759−833.

(34) Belser, P.; Dux, R.; Baak, M.; De Cola, L.; Balzani, V. *Angew. Chem., Int. Ed. Engl.* **1995**, *34*, 595−598.

(35) Balzani, V.; Scandola, F. *Supramolecular Photochemistry*; Ellis Horwood: Chichester, U.K., 1991.

(36) D'Alessandro, D. M.; Keene, F. R. *Chem. Eur. J.* **2005**, *11*, 3679−3688.

(37) Keene, F. R. *Chem. Soc. Rev.* **1998**, *27*, 185−193.

(38) Duff, C. M.; Heath, G. A. *Inorg. Chem.* **1991**, *30*, 2528−2535.

the energies (ν_{max}), intensities $\{(\epsilon/\nu)_{max}\}$ and bandwidths ($\Delta\nu_{1/2}$) were estimated as ± 10 cm^{-1}, ± 0.001 M^{-1} and ± 10 cm^{-1}, respectively.

For asymmetrically shaped IVCT bands, an examination of the moments of the band are required, rather than the experimentally observed quantities $\{\nu_{max}, (\epsilon/\nu)_{max}$ and $\Delta\nu_{1/2}\}$. The first-order moment (M_1) defines the average energy of the absorption manifold and is given by eq 4. The denominator represents the area under the band of the reduced absorption spectrum, i.e., the zeroth-moment, M_0, and $f(\nu)$ is the line-shape function of the reduced absorption spectrum $\{(\epsilon/\nu)$ vs $\nu\}$. The transition moment ($|\mu_{12}|$ in eÅ) is defined as 0.0206 Å $\times$ $M_0^{1/2}$.

$$M_1 = \left(\int_{\nu_1}^{\nu_2} f(\nu)\nu \, d\nu\right) / \left(\int_{\nu_1}^{\nu_2} f(\nu) \, d\nu\right) \tag{4}$$

IR Spectroelectrochemistry. IR spectroelectrochemistry was performed using a BioRad FTS 175C FT-IR spectrometer and the reflection/absorption−spectroelectrochemical cell described previously.[40,41] Samples were prepared using anhydrous CH$_3$CN (ca. 1.5 $\times 10^{-3}$ M complex and 0.1 M [(n-C$_4$H$_9$)$_4$N]PF$_6$ as the supporting electrolyte). The spectral characteristics of the electrogenerated mixed-valence ($+5$) species were followed by applying appropriate potentials intermediate between the two metal-based redox processes, determined from the preliminary electrochemical measurements. Following the generation of the fully oxidized ($+6$) species, the cell potential was reversed to regenerate the $+4$ species.

For selected systems, FT-IR spectra were also recorded on a Perkin-Elmer FT-IR spectrometer over the range 1000−7000 cm^{-1} using a liquid FT-IR cell which incorporated CaF$_2$ windows. The mixed-valence species were generated by chemical oxidation with NOPF$_6$ in CD$_3$CN, and their FT-IR spectra were recorded following the sequential addition of small aliquots of the oxidant to a solution of the $+4$ species (ca.3 mg in 0.5 cm^3 of CD$_3$CN).

Stark Absorption Spectroscopy. Detailed accounts of the instrumentation, sample preparation and analysis have been reported previously.[42,43] In a typical experiment, the unoxidized complex (ca. 5 mg) was dissolved in n-butyronitrile (1 cm^3) and the mixed-valence species was generated via chemical oxidation with NOPF$_6$ {saturated solution in n-butyronitrile (1 cm^3)}.

Stark absorption measurements were performed in a dual liquid nitrogen immersion cryostat (Janis Research Corporation) at 77 K.[44] The electroabsorption cell consisted of two indium−tin oxide (ITO)-coated quartz slides (Delta Technologies) separated by 100 μm Kapton spacers (DuPont). Electroabsorption measurements were performed at 77 K with a field strength of 4.0 MV cm^{-1} using a CARY-14 spectrophotometer featuring OLIS control software. Dry nitrogen gas was blown over the Dewar windows to prevent fogging. Electroabsorption measurements over the range 3850−12500 cm^{-1} were recorded with a photovoltaic HgCdTe detector that was thermoelectrically cooled to −40 °C (Judson Technologies) and a DE110 Silicon photodiode for measurements over the range 9090−20000 cm^{-1}. Stark absorption spectra for the IVCT bands of *meso*-[{Ru(bpy)$_2$}$_2$(μ-BL)]$^{5+}$ (BL = dpb, dpq′) were obtained over the range 3850−12 500 cm^{-1}, while the spectra of *meso*-[{Os-(bpy)$_2$}$_2$(μ-BL)]$^{5+}$ (BL = dpb, dpb′, dpq′, ppz) were obtained over

the range 3850−20 000 cm^{-1}. Attempts to apply the technique to *meso*-[{Ru(bpy)$_2$}$_2$(μ-BL)]$^{5+}$ (BL = dpb′, ppz) were unsuccessful due to rapid disproportionation of the mixed-valence species.

The initial analysis of the data was performed according to the method of Liptay[45] as described in detail elsewhere.[42,43,46] Briefly, each Stark spectrum {obtained from duplicate experiments at two angles (90 and 45°)} was fitted to a linear combination of the zeroth, first, and second derivatives of the absorption spectrum (at 77 K) to yield values for the coefficients, A_χ, B_χ, and C_χ in eq 5.

$$\Delta A(\nu) = \left\{ A_\chi A(\nu) + \frac{B_\chi \nu}{15hc} \frac{d[A(\nu)/\nu]}{d\nu} + \frac{C_\chi \nu}{30h^2c^2} \frac{d^2[A(\nu)/\nu]}{d\nu^2} \right\} F_{int}^2 \tag{5}$$

Here, χ is the experimental angle between $\mathbf{F}_{ext}$ and the polarization of the incident light, h is Planck's constant, and c is the speed of light in a vacuum. $\mathbf{F}_{int}$ represents the internal electric field experienced by the chromophore and is given by $f \times \mathbf{F}_{ext}$, where f is the local-field correction factor (typically assumed to be 1.3 for organic solvents,[19] although the absolute magnitude is uncertain as this depends on the chromophore and counterion concentrations). It must be noted that this approach is not strictly valid for systems which exhibit nonadiabatic electron transfer, such as those studied herein.[47]

The coefficients A_χ, B_χ, and C_χ provide information on changes in the transition dipole moment, the excited state/ground-state polarizability, and dipole moment differences, respectively, according to eq 6.

$$A_\chi = \frac{\langle\alpha_m\rangle}{3} + \frac{1}{30}(3\cos^2\chi - 1)[3\langle\beta_m\rangle - 2\langle\alpha_m\rangle]$$

$$B_\chi = \frac{5}{2}\text{Tr}(\Delta\alpha) + (3\cos^2\chi - 1)\left[\frac{3}{2}\hat{\mathbf{g}}\cdot\Delta\alpha\cdot\hat{\mathbf{g}} - \frac{1}{2}\text{Tr}(\Delta\alpha)\right]$$

$$C_\chi = |\mu_\nu|^2 [5 + (3\cos^2\xi - 1)(3\cos^2\chi - 1)] \tag{6}$$

In these equations, $\langle\alpha_m\rangle$ and $\langle\beta_m\rangle$ are the scalar functions of the transition moment polarizability and hyperpolarizability tensors, Tr-($\Delta\alpha$) is the trace of the polarizability change between the ground and excited electronic states, $\hat{\mathbf{g}}\cdot\Delta\alpha\cdot\hat{\mathbf{g}}$ is the polarizability change along the transition moment ($\hat{\mathbf{g}}$ is the unit vector), $|\mu_\nu|$ is the vector change in dipole moment (its sign is not determined), and ξ is the angle between the transition dipole moment and change in dipole moment vectors.[21] It should be noted that all values for $\hat{\mathbf{g}}\cdot\Delta\alpha\cdot\hat{\mathbf{g}}$ are quoted as $\Delta\alpha$. The Stark spectra at two or more values of χ (incident angle of polarized light in relation to the electric field) are fitted to a sum of the zeroth, first, and second derivatives of the absorption spectrum to yield values for the molecular parameters according to eq 6. It must be noted that a major contribution to the B_χ term has been omitted; however, the simplified form of the equation is valid for delocalized systems, and its use is therefore justified for the strongly electronically coupled systems reported herein.

Synthetic Procedures. 2,3-Bis(2-pyridyl)-1,4-benzoquinoxaline (dpb),[48] dipyrido(2,3-a;3′,2′−c)benzophenazine (dpb′),[28,49] and dipy-

(39) Reimers, J. R.; Hush, N. S. *Inorg. Chem.* **1990**, *29*, 3686−3697.
(40) Borg, S. J.; Best, S. P. *J. Electroanal. Chem.* **2002**, *535*, 57−64.
(41) Best, S. P.; Clark, R. J. H.; McQueen, R. C. S. *Rev. Sci. Instrum.* **1987**, *58*, 2071−2074.
(42) Karki, L.; Hupp, J. T. *Inorg. Chem.* **1997**, *36*, 3318−3321.
(43) Dinolfo, P. H.; Hupp, J. T. *J. Am. Chem. Soc.* **2004**, *126*, 16814−16819.
(44) Andrews, S. S.; Boxer, S. G. *Rev. Sci. Instrum.* **2000**, *71*, 3567−3569.

(45) Liptay, W. *Angew. Chem., Int. Ed. Engl.* **1969**, *8*, 177−188.
(46) Shin, Y.-g. K.; Brunschwig, B. S.; Creutz, C.; Sutin, N. *J. Phys. Chem.* **1996**, *100*, 8157−8169.
(47) Treynor, T. P.; Boxer, S. G., *J. Phys. Chem. A* **2004**, *108*, 1764−1778.
(48) Yeomans, B. D.; Kelso, L. S.; Tregloan, P. A.; Keene, F. R. *Eur. J. Inorg. Chem.* **2001**, 239−246.
(49) Kelso, L. S., Ph.D. Thesis, James Cook University, Townsville, Queensland, Australia, 2000.

rido(2,3-a;3′,2′-c)phenazine (dpq′)[49] were prepared according to the literature methods. 4,7-Phenanthrolino-5,6:5′,6′-pyrazine (ppz) was prepared according to a modification of the literature procedure as described previously.[29]

The mononuclear ruthenium complexes [Ru(DMSO)$_4$Cl$_2$],[50] *cis*-[Ru(pp)$_2$Cl$_2$]·2H$_2$O (pp = bpy, Me$_2$bpy),[51] *cis*-[Ru(Me$_4$bpy)$_2$Cl$_2$],[52] and *cis*-[Os(bpy)$_2$Cl$_2$]·2H$_2$O [53] were synthesized according to the literature methods.

Synthesis of Dinuclear Complexes and Separation of Diastereoisomers. A detailed account of column chromatographic procedures employed for the separation and purification of the diastereoisomers has been reported previously.[54] [{Ru(bpy)$_2$}$_2$(μ-dpb)](PF$_6$)$_4$,[28,48] [{Ru(bpy)$_2$}$_2$(μ-dpb′)](PF$_6$)$_4$,[28] [{Ru(bpy)$_2$}$_2$(μ-dpq′)](PF$_6$)$_4$,[29] and [{Ru(bpy)$_2$}$_2$(μ-ppz)](PF$_6$)$_4$[55] were synthesized and separated into the meso and rac diastereoisomers as decribed previously.

[{Ru(bpy)$_2$}$_2$(μ-2,3-dpp)](PF$_6$)$_4$. The synthesis and purification were performed under similar conditions to those described previously for [{Ru(bpy)$_2$}$_2$(μ-dpb)](PF$_6$)$_4$[28,48] involving the reaction of *cis*-[Ru(bpy)$_2$Cl$_2$]·2H$_2$O (100 mg, 0.192 mmol) with 2,3-dpp (18 mg, 0.0769 mmol). The dinuclear species was isolated as a purple solid. Yield: 122 mg (97%). Anal. Calcd for C$_{54}$H$_{42}$F$_{24}$N$_{12}$P$_4$Ru$_2$: C, 39.5; H, 2.58; N, 10.2%. Found: C, 39.3; H, 2.22; N, 10.0%.

^{1}H NMR data for the diastereoisomers are reported in the Supporting Information (Figure S1 and accompanying information).

[{Os(bpy)$_2$}$_2$(μ-dpb)](PF$_6$)$_4$. A suspension of dpb (25 mg, 0.0747 mmol) in ethylene glycol (1.5 cm^3) was heated in a modified microwave oven on medium-high power for 20 s to complete dissolution. *cis*-[Os(bpy)$_2$Cl$_2$]·2H$_2$O (94.3 mg, 0.155 mmol) was added, and the mixture heated at reflux for a further 5 min on high power during which time the solution attained a dark green coloration. The crude mixture was diluted with distilled water (50 cm^3) and loaded onto a column of SP Sephadex C-25 (dimensions 25 cm × 3 cm). Separation of the desired dinuclear product from the mixture was achieved via gradient elution procedure with aqueous NaCl solution as the eluent. A purple band of mononuclear material eluted first (0.2 M NaCl) followed by the desired dark green product (0.4 M NaCl), which was precipitated as the PF$_6^-$ salt by addition of a saturated solution of aqueous KPF$_6$. The solid was isolated by vacuum filtration and washed with diethyl ether (3 × 10 cm^3). Yield: 131 mg (92%). Anal. Calcd for C$_{62}$H$_{46}$F$_{24}$N$_{12}$P$_4$Os$_2$: C, 38.8; H, 2.42; N, 8.75%. Found: C, 38.6; H, 2.41; N, 8.67%. Further characterization was performed following diastereoisomer separation.

Separation of the diastereoisomers was achieved using an SP Sephadex C-25 support with aqueous 0.25 M sodium toluene-4-sulfonate solution as the eluent.[56] Bands 1 and 2 were determined to be the meso and rac diastereoisomers, respectively, as established by X-ray crystallography and NMR characterization. ^{1}H NMR data for the diastereoisomers are reported in the Supporting Information (Figure S2 and accompanying information).

[{Os(bpy)$_2$}$_2$(μ-dpb′)](PF$_6$)$_4$. The synthesis, diastereoisomeric separation, and purification were performed via a similar procedure to that described above for [{Os(bpy)$_2$}$_2$(μ-dpb)](PF$_6$)$_4$ involving the reaction of *cis*-[Os(bpy)$_2$Cl$_2$]·2H$_2$O (114 mg, 0.187 mmol) with dpb′ (30 mg, 0.0903 mmol). The dinuclear species was isolated as an olive green solid. Yield: 147 mg (85%). Anal. Calcd for C$_{62}$H$_{44}$F$_{24}$N$_{12}$P$_4$Os$_2$: C, 38.8; H, 2.31; N, 8.77%. Found: C, 38.5; H, 2.46; N, 8.53%.

^{1}H NMR data for the diastereoisomers are reported in the Supporting Information (Figure S3 and accompanying information).

[{Os(bpy)$_2$}$_2$(μ-dpq′)](PF$_6$)$_4$. The synthesis and purification were performed under similar conditions to those described above for [{Os(bpy)$_2$}$_2$(μ-dpb)](PF$_6$)$_4$ involving the reaction of *cis*-[Os(bpy)$_2$Cl$_2$]·2H$_2$O (100 mg, 0.164 mmol) with dpq′ (22.3 mg, 0.0791 mmol). The dinuclear species was isolated as a dark green solid. Yield: 145 mg (98%). Anal. Calcd for C$_{58}$H$_{42}$F$_{24}$N$_{12}$P$_4$Os$_2$: C, 37.3; H, 2.27; N, 9.00%. Found: C, 37.0; H, 2.15; N, 8.87%.

^{1}H NMR data for the diastereoisomers are reported in the Supporting Information (Figure S4 and accompanying information).

[{Os(bpy)$_2$}$_2$(μ-ppz)](PF$_6$)$_4$. The synthesis and purification were performed under similar conditions to those described above for [{Os(bpy)$_2$}$_2$(μ-dpb)](PF$_6$)$_4$ involving the reaction of *cis*-[Os(bpy)$_2$Cl$_2$]·2H$_2$O (54.3 mg, 0.0947 mmol) with ppz (10 mg, 0.0431 mmol). The dinuclear species was isolated as a turquoise solid. Yield: 60 mg (77%). Anal. Calcd for C$_{54}$H$_{40}$F$_{24}$N$_{16}$P$_4$Os$_2$: C, 34.6; H, 2.15; N, 12.0%. Found: C, 34.4; H, 2.28; N, 11.8%.

^{1}H NMR data for the diastereoisomers are reported in the Supporting Information (Figure S5 and accompanying information).

[{Os(bpy)$_2$}$_2$(μ-2,3-dpp)](PF$_6$)$_4$. The synthesis and purification were performed under similar conditions to those described above for [{Os(bpy)$_2$}$_2$(μ-dpb)](PF$_6$)$_4$ involving the reaction of *cis*-[Os(bpy)$_2$Cl$_2$]·2H$_2$O (94.3 mg, 0.164 mmol) with 2,3-dpp (17.5 mg, 0.0747 mmol). The dinuclear species was isolated as a dark purple solid. Yield: 130 mg (96%). Anal. Calcd for C$_{54}$H$_{42}$F$_{24}$N$_{12}$P$_4$Os$_2$: C, 35.7; H, 2.33; N, 9.24%. Found: C, 35.5; H, 2.14; N, 9.20%.

^{1}H NMR data for the diastereoisomers are reported in the Supporting Information (Figure S6 and accompanying information).

X-ray Crystallography. Single crystals of *meso*-[{Os(bpy)$_2$}$_2$-(μ-dpb)](ZnCl$_4$)$_2$·6H$_2$O were obtained by initially stirring a suspension of the hexafluorophosphate salt (10 mg) in distilled water (1 cm^3) with DOWEX anion-exchange resin (Cl$^-$ form) to afford the corresponding chloride salt. Following the addition of 2 molar equivalents of ZnCl$_2$ and aqueous HCl (3 drops, 2 M), the solutions were allowed to evaporate slowly at room temperature to yield deep green rod-shaped crystals of *meso*-[{Os(bpy)$_2$}$_2$(μ-dpb)](ZnCl$_4$)$_2$·6H$_2$O suitable for X-ray determination. Deep green, octahedral-shaped crystals of *meso*-[{Os(bpy)$_2$}$_2$(μ-dpq′)](PF$_6$)$_4$ were grown by slow evaporation of a 70:30 2,2,2-trifluoroethanol/H$_2$O solution (1.5 cm^3) of the complex under ambient conditions in the absence of light.

The collection and refinement of X-ray data was performed in the Advanced Analytical Center at James Cook University. Hemispheres of data were collected (on crystals coated with polyacrylamide glue) at room temperature on a Bruker SMART CCD diffractometer using the ω scan mode. A summary of the data collection and refinement details is provided in Table S1, Supporting Information. Data sets were corrected for absorption using the program SADABS.[56] The solution and refinement for all structures was carried out using SHELXL-97[58] utilizing the graphical interface WinGX.[59]

(50) Evans, I. P.; Spencer, A.; Wilkinson, G. *J. Chem. Soc., Dalton Trans.* **1973**, 204−209.
(51) Togano, T.; Nagao, N.; Tsuchida, M.; Kumakura, H.; Hisamatsu, K.; Howell, F. S.; Mukaida, M. *Inorg. Chim. Acta* **1992**, *195*, 221−225.
(52) Anderson, P. A.; Anderson, R. F.; Furue, M.; Junk, P. C.; Keene, F. R.; Patterson, B. T.; Yeomans, B. D. *Inorg. Chem.* **2000**, *39*, 2721−2728.
(53) Buckingham, D. A.; Dwyer, F. P.; Goodwin, H. A.; Sargeson, A. M. *Aust. J. Chem.* **1964**, *17*, 325−336.
(54) Fletcher, N. C.; Junk, P. C.; Reitsma, D. A.; Keene, F. R. *J. Chem. Soc., Dalton Trans.* **1998**, 133−138.
(55) D'Alessandro, D. M.; Keene, F. R. *Dalton Trans.* **2006**, 1060−1072.
(56) Fletcher, N. C.; Ward, M. D.; Encinas, S.; Armaroli, N.; Flamigni, L.; Barigelletti, F. *Chem. Commun.* **1999**, 2089−2090.

(57) Blessing, R. H. *Acta Crystallogr.* **1995**, *A51*, 33−38.
(58) Sheldrick, G. M. *SHELXL-97*; Institute for Anorganische Chemie der Universität Gottingen: Gottingen, 1997.

Results and Discussion

Diastereoisomer Synthesis, Separation, and Structural Characterization. The complexes $[\{Ru(bpy)_2\}_2(\mu\text{-BL})]^{4+}$ (BL = dpb, dpb′, dpq′, ppz, 2,3-dpp, 2,5-dpp) and $[\{Os(bpy)_2\}_2(\mu\text{-BL})]^{4+}$ (BL = dpb, dpb′, dpq′, ppz, 2,3-dpp) were synthesized by the reaction of 2.2 equiv of *cis*-$[M(bpy)_2Cl_2]$ (M = Ru or Os) with the bridging ligand in ethylene glycol, using the microwave-assisted methodology which is well established for the synthesis of a range of mono-,[52,60,61] di-,[28,48,49,54,61] and trinuclear[61,62] polypyridyl complexes of ruthenium and osmium. This technique produced equivalent or increased reaction yields of the dinuclear species compared with thermal methods previously reported for the syntheses of $[\{Ru(bpy)_2\}_2(\mu\text{-BL})]^{4+}$ (BL = dpb,[63] ppz,[64,65] 2,3-dpp,[66-71]) and $[\{Os(bpy)_2\}_2(\mu\text{-BL})]^{4+}$ (BL = dpb, 2,3-dpp),[66,72-74] and with significantly reduced reaction times.

The separation of the diastereoisomeric forms of the dinuclear complexes was achieved by cation-exchange chromatography using SP Sephadex C-25 as the support with aqueous solutions of sodium toluene-4-sulfonate as the eluent. In all cases, the Band 1 and 2 eluates were determined to be the meso and rac diastereoisomers, respectively: X-ray crystallography and ¹H NMR analyses permitted unambiguous characterization of the separated diastereoisomers.

¹H NMR Studies. The assignments of the ¹H NMR spectra for the series of dinuclear ruthenium complexes have been reported previously.[28,29,55] The assignments for the dinuclear osmium complexes were conducted with the assistance of ¹H COSY spectra and were based on their ruthenium analogues, allowing for the slight upfield shift of the proton resonances due to the increased shielding influence of the Os center compared with Ru.[26]

The ¹H numbering schemes for the diastereoisomers of the complexes used in this study are given in Figures S1−S6 of the Supporting Information, together with the ¹H NMR data. In all cases, the coordinated bpy ligands exhibited the expected coupling constant values[75] ($J_{3,4}$ = 8 Hz, $J_{3,5}$ = 1.5 Hz, $J_{4,5}$ = 8 Hz, $J_{4,6}$ = 1.5 Hz, and $J_{5,6}$ = 5 Hz) and coupling patterns based on the symmetry requirements of the complexes.

$[\{Os(bpy)_2\}_2(\mu\text{-dpb}′)]^{4+}$. The meso and rac diastereoisomers may be distinguished on the basis of differential anisotropic interactions experienced by the bpy protons, which depend on the stereochemical relationship of the two metal centers. The point group symmetries of both diastereoisomers (C_s and C_2, respectively) require two nonequivalent bpy ligands, with the two halves of each being magnetically nonequivalent. This gives rise to four different environments for the pyridyl rings (denoted rings a−d in Figure S3): two over the bridge (rings b and d) and two directed away from the bridge (rings a and c). In addition, the dpb′ ligand exhibits seven magnetically nonequivalent proton resonances.

The H5 and H6 protons (rings b and d oriented over the bridge) experience the most pronounced shifts between the two diastereoisomeric forms. In the rac diastereoisomer, bpy ring b is oriented over the plane of the dpb ligand and the bpy ligand across the bridge such that the H5 and H6 protons of this ring experience increased diamagnetic anisotropic effects. The H5 proton of ring b was assigned as the most upfield resonance at 6.93 ppm (J = 8, 5 Hz, dd) while H6 (ring b) was assigned as the 7.36 ppm (J = 5, 1.5 Hz, dd) resonance. By comparison, in the meso diastereoisomer the H5 and H6 protons of bpy ring b are oriented approximately in the plane and thus in the deshielding cone of the equivalent bpy across the bridge. As a result, the H5′ proton of ring d, which is situated over the plane of the dpb′ ligand and approximately parallel to the magnetically equivalent bpy across the bridge, experiences the greatest anisotropic effect and is assigned as the most upfield resonance at 7.12 ppm (J = 8, 5 Hz, dd).

$[\{Os(bpy)_2\}_2(\mu\text{-BL})]^{4+}$ (BL = dpb, dpq′, ppz, 2,3-dpp). The ¹H NMR spectra for a given diastereoisomer exhibit comparable features over the series of complexes, which are consistent with the symmetry requirements of the complexes {C_s (meso) and C_2 (rac)} and the variation in the number of resonances due to the bridging ligands. The chemical shift assignments were performed with the assistance of ¹H COSY spectra and by comparison with the spectral assignments for $[\{Os(bpy)_2\}_2(\mu\text{-dpb}′)]^{4+}$.

The diastereoisomers of $[\{Os(bpy)_2\}_2(\mu\text{-dpb})]^{4+}$ exhibit broader ¹H NMR spectra than their dpb′-bridged analogues. Steric interactions between the H13 and H14 protons of the two pyridyl rings of dpb (Figure S2, Supporting Information) induce a structural distortion in the bridging ligand by forcing the rings to move out of the plane of the bridge. This distortion gives rise to conformational isomers that interchange slowly on the NMR time scale at room temperature, with the resultant spectral broadening being greater for the meso diastereoisomer than for the rac form. A similar observation has been reported for the related system $[\{Ru(bpy)_2\}_2(\mu\text{-2,3-dpp})]^{4+}$.[37] For the diastereoisomers incorporat-

(59) Farrugia, L. J. *J. Appl. Crystallogr.* **1999**, *32*, 837−838.
(60) Jandrasics, E. Z.; Keene, F. R. *J. Chem. Soc., Dalton Trans.* **1997**, 153−159.
(61) Rutherford, T. J.; Van Gijte, O.; Kirsch − De Mesmaeker, A.; Keene, F. R. *Inorg. Chem.* **1997**, *36*, 4465−4474.
(62) Rutherford, T. J.; Keene, F. R. *J. Chem. Soc., Dalton Trans.* **1998**, 1155−1162.
(63) Molnar, S. M.; Neville, K. R.; Jensen, G. E.; Brewer, K. J. *Inorg. Chim. Acta* **1993**, *206*, 69−76.
(64) Fuchs, Y.; Lofters, S.; Dieter, T.; Shi, W.; Morgan, T. C.; Strekas, T. C.; Gafney, H. D.; Baker, A. D. *J. Am. Chem. Soc.* **1987**, *109*, 2691−2697.
(65) Morgan, O.; Wang, S.; Bae, S.-A.; Morgan, R. J.; Baker, A. D.; Strekas, T. C.; Engel, R. *J. Chem. Soc., Dalton Trans.* **1997**, 3773−3776.
(66) Denti, G.; Campagna, S.; Sabatino, L.; Serroni, S.; Ciano, M.; Balzani, V. *Inorg. Chem.* **1990**, *29*, 4750−4758.
(67) Wallace, A. W.; Murphy, W. R.; Petersen, J. D. *Inorg. Chim. Acta* **1989**, *166*, 47−54.
(68) Scott, S. M.; Gordon, K. C. *Inorg Chim Acta* **1997**, *254*, 267−272.
(69) Johnson, J. E. B.; Ruminski, R. R. *Inorg. Chim. Acta* **1993**, *208*, 231−237.
(70) Braunstein, C. H.; Baker, A. D.; Strekas, T. C.; Gafney, H. D. *Inorg. Chem.* **1984**, *23*, 857−864.
(71) Rillema, P.; Mack, K. B. *Inorg. Chem.* **1982**, *21*, 3849−3854.
(72) Richter, M. M.; Brewer, K. J. *Inorg. Chem.* **1993**, *32*, 2827−2834.
(73) Richter, M. M.; Brewer, K. J. *Inorg. Chim. Acta* **1991**, *180*, 125−131.
(74) Richter, M. M.; Brewer, K. J. *Inorg. Chem.* **1992**, *31*, 1594−1598.

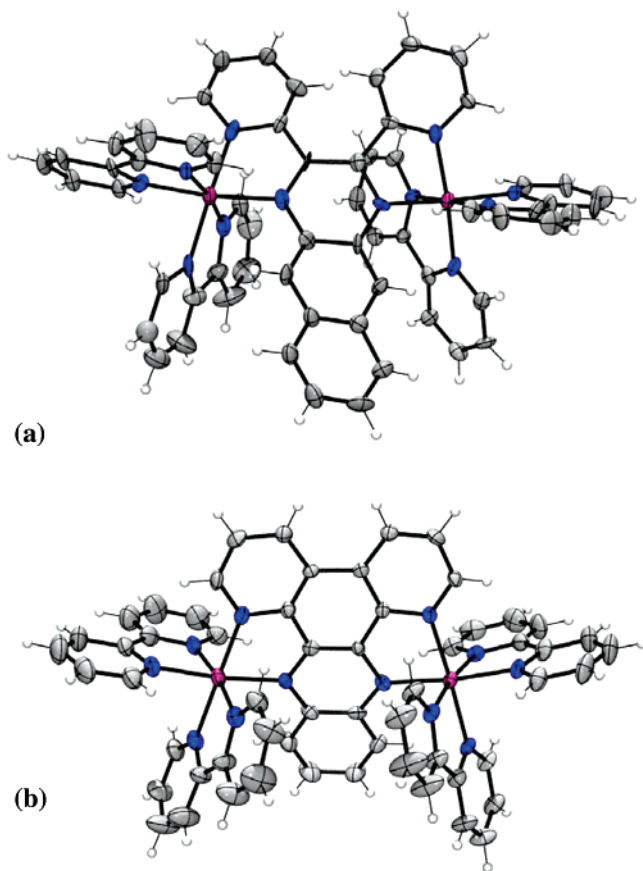(75) Constable, E. C.; Lewis, J. *Inorg. Chim. Acta* **1983**, *70*, 251−253.

(a)

(b)

Figure 3. ORTEP structures of the cations in (a) *meso*-(ΛΔ)-[{Os(bpy)$_2$}$_2$-(μ-dpb)](ZnCl$_4$)$_2$·6H$_2$O and (b) *meso*-(ΛΔ)-[{Os(bpy)$_2$}$_2$(μ-dpq′)](PF$_6$)$_4$.

ing the "fused" bridging ligand dpb′, the rigidity precludes such conformational lability. Despite the broadening of the resonances in the complexes incorporating the "unfused" dpb bridging ligand, the diastereoisomeric forms of the complex exhibit distinctive resonances which permit their characterization.

Structural Considerations: X-ray Crystallography. *meso*-(ΛΔ)-[{Os(bpy)$_2$}$_2$(μ-dpb)](ZnCl$_4$)$_2$·6H$_2$O crystallized in the monoclinic space group $P2_1/c$ with four dinuclear cations in the unit cell, and *meso*-(ΛΔ)-[{Os(bpy)$_2$}$_2$(μ-dpq′)]-(PF$_6$)$_4$ crystallized in the orthorhombic space group *Pbca* with eight dinuclear cations in the unit cell. The perspective views of the dinuclear cations are shown in Figure 3a and b.

The nature of the distortions in the crystal structures of *meso*-(ΛΔ)-[{Os(bpy)$_2$}$_2$(μ-dpb)]$^{4+}$ and *meso*-(ΛΔ)-[{Os-(bpy)$_2$}$_2$(μ-dpq′)]$^{4+}$ are comparable with those observed in their ruthenium analogues.[29] For *meso*-(ΛΔ)-[{Os(bpy)$_2$}$_2$-(μ-dpb)]$^{4+}$ shown in Figure 3a, steric hindrance between the H13 and H14 protons (Figure S7, Supporting Information) forces the two pyridyl rings to twist out of the central plane. The dpb bridging ligand exhibits considerable distortion in the central pyrazine ring in addition to a large dihedral skew of the two pyridyl ligands and a twist in the benzoquinoxaline "tail" of the bridge. In *meso*-(ΛΔ)-[{Os(bpy)$_2$}$_2$(μ-dpq′)]$^{4+}$, the C−C bond linking the two pyridyl rings of the bridging ligand in dpq′ prevents such lateral movements. The slight curvature of the bridging ligand shown in Figure 3b arises

from unfavorable steric interactions between the equatorial hydrogen atoms on the phenazine "tail" of the bridging ligand and the terminal bpy rings oriented parallel to the long axis of the bridge.

In both structures, the metal centers reside in distorted octahedral environments and the degree of structural distortion is more pronounced for the dpb-bridged complex. The average "bite angles" subtended by the Os centers and nitrogen atoms of the bridging ligand are 77.2(3)° and 78.6-(3)° for the dpb- and dpq′-bridged structures, respectively, consistent with the results for their ruthenium analogues and with those published previously for polypyridyl complexes of osmium.[54,76−81] For the dpb-bridged structure, the average Os−N(pyrazine) and Os−N(pyridine) bond lengths are 2.038(5) and 2.050(5) Å, while the average bond lengths are 2.060(5) and 2.061(5) Å, respectively, for the dpq′-bridged structure. The slight shortening of the Os−N distances compared with the Ru−N bond lengths in their ruthenium analogues reflects the enhanced π-back-bonding interactions for Os(II) compared with Ru(II). Such observations have been noted previously in the comparison of the isostructural ruthenium and osmium derivatives of the fully oxidized forms of the Creutz−Taube ion, [{Os(NH$_3$)$_5$}$_2$(μ-pyz)]Cl$_6$·2H$_2$O.[82] In the present case, the Os(1)···Os(2) distances are 6.823(5) and 6.837(8) Å for the dpb- and dpq′-bridged structures, respectively, which are comparable to the distances 6.856(2) and 6.818(1) Å in the crystal structures of *meso*-[{Ru(bpy)$_2$}$_2$(μ-dpb)](ZnCl$_4$)$_2$·5H$_2$O and *meso*-[{Ru-(bpy)$_2$}$_2$(μ-dpq′)](ZnCl$_4$)$_2$·3H$_2$O, respectively.[29]

Electrochemical and UV/vis/NIR Spectral Characterization. The redox potentials for the E_{ox1} ([5+/4+]; i.e., Ru^{III}−Ru^{II}/Ru^{II}−Ru^{II}) and E_{ox2} ([6+/5+]; i.e., Ru^{III}−Ru^{III}/Ru^{III}−Ru^{II}) couples for the series of complexes *meso*- and *rac*-[{M(bpy)$_2$}$_2$(μ-BL)]$^{4+}$ (M = Ru, Os; BL = dpb, dpb′, dpq′, ppz, 2,3-dpp) were investigated by cyclic and differential pulse voltammetry in acetonitrile/0.1 M [(n-C$_4$H$_9$)$_4$N]-PF$_6$ solution and are reported in Table 1. The full details of the electrochemical properties and the complete UV/vis/NIR spectral data for the diastereoisomeric forms of the osmium species [{Os(bpy)$_2$}$_2$(μ-BL)]$^{n+}$ (n = 4, 5, 6) are reported in Tables S2 and S3 (Supporting Information), respectively, and the corresponding data for the ruthenium analogues in Tables S4 and S5. ΔE$_{ox}$ defines the potential difference between the [6+/5+] and [5+/4+] couples.

The dinuclear systems are each characterized by two reversible one-electron redox processes corresponding to

(76) Bardwell, D.; Jeffery, J. C.; Joulie, L.; Ward, M. D. *J. Chem. Soc., Dalton Trans.* **1993**, 2255−2256.
(77) Bardwell, D. A.; Horsburgh, L.; Jeffery, J. C.; Joulié, L. F.; Ward, M. D.; Webster, I.; Yellowlees, L. J. *J. Chem. Soc., Dalton Trans.* **1996**, 2527−2531.
(78) Hage, R.; Haasnoot, J. G.; Nieuwenhuis, H. A.; Reedijk, J.; De Ridder, D. J. A.; Vos, J. G. *J. Am. Chem. Soc.* **1990**, *112*, 9245−9251.
(79) Balzani, V.; Bardwell, D. A.; Barigelletti, F.; Cleary, F. L.; Guardigli, M.; Jeffery, J. C.; Sovrani, T.; Ward, M. D. *J. Chem. Soc., Dalton Trans.* **1995**, 3601−3608.
(80) Baitalik, S.; Flörke, U.; Nag, K. *J. Chem. Soc, Dalton Trans.* **1999**, 719−727.
(81) Masui, H.; Freda, A. L.; Zerner, M. C.; Lever, A. B. P. *Inorg. Chem.* **2000**, *39*, 141−152.
(82) Bino, A.; Lay, P. A.; Taube, H.; Wishart, J. F. *Inorg. Chem.* **1985**, *24*, 4, 3969−3971.

Table 1. Electrochemical Data (in mV relative to the Fc^+/Fc^0 Couple) and K_c Values[a] for the Diastereoisomers of $[\{M(bpy)_2\}_2(\mu\text{-}BL)]^{4+}$ (M = Ru, Os) in 0.1 M $[(n\text{-}C_4H_9)_4N]PF_6/CH_3CN$[b]

BL	diastereoisomer	M = Ru				M = Os			
		$K_c\ (\times 10^{-3})$	ΔE_{ox}	E_{ox2}	E_{ox1}	$K_c\ (\times 10^{-3})$	ΔE_{ox}	E_{ox2}	E_{ox1}
dpb	meso	2.06	196	1280	1084	256	320	956	636
	rac	0.944	176	1280	1104	86.2	292	944	652
dpb′	meso	8.35	232	1300	1068	3616	388	988	600
	rac	6.11	224	1304	1080	4225	392	992	604
dpq′	meso	2.40	200	1285	1085	1040	356	960	608
	rac	2.40	200	1297	1097	1660	368	976	616
ppz	meso	6.11	224	1280	1056	890	352	916	568
	rac	4.48	216	1278	1062	1040	356	924	568
2,3-dpp	meso	3.83	212	1256	1044	378	330	924	594
	rac	3.83	212	1244	1032	237	318	912	594

[a] K_c values are given by $K_c = \exp(\Delta E_{ox}F/RT)$ where $F/RT = 38.92$ V^{-1} at 298 K. [b] $\Delta E_{ox} = E_{ox2} - E_{ox1}$. Potentials are quoted ±3 mV.

successive oxidations of the metal centers in addition to multiple reversible ligand-based reductions in the cathodic region. In the cathodic region, the first two processes are assigned to the successive one-electron reductions of the bridging ligands ($BL^{0/-}$ and $BL^{-/2-}$) which is consistent with the stronger π-acceptor nature of the bridging relative to the terminal bpy ligands.[63,66-71,83-86] The subsequent four one-electron processes correspond to successive reduction of the terminal bpy ligands. The cathodic shift of E_{red1} and E_{red2} as the bridging ligand is varied through the series ppz, dpb, dpq′, dpb′, and 2,3-dpp is consistent with the stabilization of the π^*(BL) lowest unoccupied molecular orbitals (LUMOs). By comparison, the potentials for the bpy-based reductions remain relatively constant with bridging ligand variation. E_{ox1} and E_{ox2} for the osmium species are shifted cathodically by approximately 500 mV relative to the corresponding metal-based processes in their dinuclear ruthenium analogues due to the raised $d\pi$ level of Os compared with Ru.[26,66,72,73,87]

Differences in the values of ΔE_{ox} are observed between the different complexes, with the magnitude increasing as BL is varied through the series dpb, ppz, dpq′, 2,3-dpp, and dpb′. There are also variations between the diastereoisomeric forms of the each complex, the largest difference being observed for $[\{M(bpy)_2\}_2(\mu\text{-}dpb)]^{4+}$. The presence of structural distortions in the dpb-bridged diastereoisomers may explain the significant difference between their ΔE_{ox} values, as well as the lower magnitudes of ΔE_{ox} relative to the other complexes of the series. However, the differences cannot be ascribed solely to variations in the extent of electronic delocalization, as the magnitude of ΔE_{ox} also reflects contributions from ion-pairing interactions,[88] solvation energies, and statistical factors.[87,89] In addition, the ΔE_{ox} values are increased by 115-135 mV for the osmium relative to the ruthenium dpb-bridged dinuclear complexes, which results in a two-orders-of-magnitude increase in K_c for the

former: the enhanced stability of the mixed-valence osmium species arises predominantly from the relatively greater degree of metal-ligand back-bonding.[87,90]

The UV/vis/NIR spectral data for the unoxidized (+4), mixed-valence (+5), and fully oxidized (+6) forms of $[\{Ru(bpy)_2\}_2(\mu\text{-}BL)]^{4+}$ (for the range 3050-30 000 cm^{-1}) have been detailed previously.[29] The spectra are characterized by a combination of overlapping $d\pi(Ru^{II}) \rightarrow \pi^*$(BL, bpy) singlet metal-to-ligand (^{1}MLCT) transitions. The lowest-energy absorption band shifts to the red as BL is varied through the series 2,3-dpp, ppz, dpb, dpq′, and dpb′, consistent with the increasing stabilization of the π^*(BL) orbitals. The mixed-valence state was characterized by IVCT bands in the region 3500-9000 cm^{-1}.

The spectra of the analogous $[\{Os(bpy)_2\}_2(\mu\text{-}BL)]^{4+}$ series exhibit similar features in the region 15 000-30 000 cm^{-1} which are assigned as overlapping $d\pi(Os^{II}) \rightarrow \pi^*$(BL) and $d\pi(Os^{II}) \rightarrow \pi^*$(bpy) ^{1}MLCT transitions, consistent with previous literature reports for the complexes $[\{Os(bpy)_2\}_2(\mu\text{-}BL)]^{4+}$ (BL = dpb and 2,3-dpp) as diastereoisomeric mixtures.[66,72,73,87] The lowest-energy absorption band is assigned as a $d\pi(Os^{II}) \rightarrow \pi^*$(BL) transition to the lowest, triplet excited state (^{3}MLCT). This band undergoes a red-shift as BL is varied through the series 2,3-dpp, ppz, dpb, dpq′, and dpb′, consistent with the increasing stabilization of the π^*(BL) orbitals.[66,72-74,87] For the series of dinuclear osmium complexes, the expected 1:1 energy correlation between $E_{ox1-red1}$ and the energies of ^{1}MLCT and ^{3}MLCT transitions[91-94] was confirmed (meso: $R^2 = 0.998$ for ^{1}MLCT and 0.983 for ^{3}MLCT; rac: $R^2 = 0.997$ for ^{1}MLCT and 0.951 for ^{3}MLCT).

The UV/vis/NIR spectra for the diastereoisomers of the osmium series of complexes at -35 °C are provided in Figure S9. Spectroelectrochemical generation of the +5 and +6 forms of the diastereoisomers revealed stable isosbestic points in the spectral progressions accompanying both

(83) Berger, R. M. *Inorg. Chem.* **1990**, *29*, 1920-1924.
(84) Seneviratne, D. S.; Uddin, M. J.; Swayambunathan, V.; Schlegel, H. B.; Endicott, J. F. *Inorg. Chem.* **2002**, *41*, 1502-1517.
(85) Giuffrida, G.; Campagna, S. *Coord. Chem. Rev.* **1994**, *135*, 517-531.
(86) Juris, A.; Barigelletti, S.; Campagna, S.; Balzani, V.; Belser, P.; von Zelewsky, A. *Coord. Chem. Rev.* **1988**, *84*, 85-277.
(87) Goldsby, K. A.; Meyer, T. J. *Inorg. Chem.* **1984**, *23*, 3002-3010.
(88) D'Alessandro, D. M.; Keene, F. R. *Dalton Trans.* **2004**, 3950-3954.
(89) Richardson, D. E.; Taube, H. *J. Am. Chem. Soc.* **1983**, *105*, 40-51.

(90) Richardson, D. E.; Taube, H. *Coord. Chem. Rev.* **1984**, *60*, 107-129.
(91) Kober, E. M.; Sullivan, B. P.; Dressick, W. J.; Caspar, J. V.; Meyer, T. J. *J. Am. Chem. Soc.* **1980**, *102*, 7383-7385.
(92) Caspar, J. V.; Kober, E. M.; Sullivan, B. P.; Meyer, T. J. *J. Am. Chem. Soc.* **1982**, *104*, 630-632.
(93) Dodsworth, E. S.; Lever, A. B. P. *Chem. Phys. Lett.* **1985**, *119*, 61-66.
(94) Saji, T.; Aoyagui, S. *J. Electroanal. Chem.* **1975**, *60*, 1-10.

Table 2. IVCT Spectral Data of the Reduced Absorption Spectra (ϵ/ν vs ν) for the Diastereoisomeric Forms of [{Ru(bpy)$_2$}$_2$(μ-BL)]$^{5+}$ (BL = dpb, dpb′, dpq′, Ppz) in 0.1 M [(n-C$_4$H$_9$)$_4$N]PF$_6$/CH$_3$CN at −35 °C and Parameters Derived from the Moment Analysis of the Transitions[a]

BL	diastereoisomer	ν_{max}/cm^{-1}	$(\epsilon/\nu)_{max}$/M^{-1}	$\Delta\nu_{1/2}$/cm^{-1}	M_0/M^{-1}	M_1/cm^{-1}	$|\mu_{12}|$/eÅ	$\Delta\nu_{1/2}°$/cm^{-1}
dpb	meso	5205	0.3062	1910	639.8	5655	0.5211	3090
	rac	5000	0.4572	1740	870.5	5450	0.6078	3030
dpb′	meso	5285	0.8084	1070	1010	5510	0.6546	3115
	rac	5290	0.7222	1080	903.2	5510	0.6190	3115
dpq′	meso	5195	0.5934	1710	1140	5600	0.6955	3090
	rac	5220	0.6329	1450	1050	5600	0.6675	3100
ppz	meso	5370	0.8721	1560	1680	5930	0.8440	3140
	rac	5390	0.8494	1560	1680	5960	0.8440	3150

[a] The errors in the observed parameters are ±10 cm^{-1} for ν_{max}, M_1, and $\Delta\nu_{1/2}$, ±0.001 M^{-1} for $(\epsilon/\nu)_{max}$, ±5 M^{-1} for M_0, and ±0.001 eÅ for $|\mu_{12}|$.

oxidation processes. The ^{1}MLCT absorption bands decreased in intensity on one-electron oxidation and disappeared on further oxidation to the +6 species. While the energies of these transitions remain approximately constant upon oxidation for the dpb- and dpb′-bridged complexes, the bands experience a blue-shift upon oxidation in the complexes bridged by dpq′, ppz, and 2,3-dpp: the latter behavior may be indicative of valence delocalization.[95] By contrast, the ^{1}MLCT bands experience red-shifts upon oxidation from the +4 to the +5 species in the ruthenium complexes, which suggests that they may be relatively less localized.

The ^{3}MLCT absorption bands decreased in intensity upon oxidation, and small differences were observed in the energies and intensities of these transitions between the diastereoisomeric forms of the same complex. A notable feature of the spectra was the narrower ^{3}MLCT and ^{1}MLCT bands for the complexes incorporating the fused bridging ligands dpb′ and ppz relative to their unfused analogues (dpb and 2,3-dpp, respectively).

NIR and Mid-IR Spectroelectrochemistry. Dinuclear Ruthenium Complexes. The IVCT properties for the diastereoisomers of [{Ru(bpy)$_2$}$_2$(μ-BL)]$^{4+}$ have been discussed previously,[29] and an overlay of the IVCT bands for the full series of complexes is shown in Figure S10 (Supporting Information); the results of the band maxima (ν_{max}), molar absorption coefficients {$(\epsilon/\nu)_{max}$}, and bandwidths ($\Delta\nu_{1/2}$) are summarized in Table 2. For all complexes, the bands are asymmetrically shaped and narrower on the lower-energy side. The results for the first-order moment analysis[2,39] are also presented in Table 2, where the zeroth- (M_0) and first-order (M_1) moments represent the band area and average band energy, respectively, and $|\mu_{12}|$ is the transition moment.

A classical two-state analysis[5] of the IVCT transitions revealed that all the systems exhibit significant electronic delocalization. On the basis of the narrow bandwidths compared with the theoretical values ($\Delta\nu_{1/2}° =$ [16RT ln 2(ν_{max})]$^{1/2}$, where 16RT ln 2 = 1836 cm^{-1} at 238 K), the systems lie close to the localized-to-delocalized transition. From the moment analysis of the bands, the general trend is an increase in the extent of delocalization for the fused bridging ligands as BL is varied from dpb′ to dpq′ to ppz.[29]

The differences in the IVCT parameters {specifically, $(\epsilon/\nu)_{max}$, M_0, and $|\mu_{12}|$} reported in Table 2 suggest that the extent of electronic coupling differs for the diastereoisomeric forms of the same complex. Interestingly, while the IVCT energies (ν_{max} or M_1) are identical within experimental error for the diastereoisomers incorporating the series of fused bridges (dpb′, dpq′, ppz), the unfused dpb-bridged forms exhibit a 205 cm^{-1} difference in energies. This difference is attributed to the presence of a differential structural distortion in the dpb bridging ligand,[29] and may be regarded as a redox asymmetry contribution to the electron-transfer barrier (denoted by ΔE_{struct}).

The theoretical analysis of the IVCT data for the borderline localized-to-delocalized systems[29] is challenging since the application of classical models[2,3,16,96] is invalid because of the failure to meet the Born−Oppenheimer approximation upon which they are based.[14,16] As a consequence of the inapplicability of the two-state model, the H_{ab} values could not be reliably determined from eq 2 and are not reported in Table 2.

Dinuclear Osmium Complexes. The NIR spectra for the mixed-valence complexes *meso-* and *rac-*[{Os(bpy)$_2$}$_2$(μ-BL)]$^{5+}$ (BL = dpb′, dpq′, ppz, dpb, 2,3-dpp) are shown in Figure S9 (Supporting Information), and the results for the band parameters {ν_{max} and $(\epsilon/\nu)_{max}$} are summarized in Table 3. Due to the convoluted nature of the spectra, the $\Delta\nu_{1/2}$ values for the absorption bands were obtained by Gaussian deconvolution and are reported in Tables S6 and S7. Figure S9 shows the overlays of the NIR spectra for *meso-* and *rac-* [{Os(bpy)$_2$}$_2$(μ-BL)]$^{n+}$ (n = 5, 6).

The NIR spectra of the dinuclear osmium systems exhibit an added complexity in behavior compared to their ruthenium analogues due to the larger spin−orbit coupling constant for Os ($\xi_{Os} \approx 3000$ cm^{-1} cf. $\xi_{Ru} \approx 1000$ cm^{-1}). While the maxima of the IVCT bands in the ruthenium complexes occur in the same region (5000−5400 cm^{-1}, Table 2), the patterns of the energies, intensities, and bandwidths of the multiple IVCT and IC transitions differ markedly within the series of osmium complexes. However, the NIR spectra of the two pairs of complexes bridged by ppz and 2,3-dpp and the complexes bridged by dpq′ and dpb display a close resemblance to one another in each case.

The first oxidation process for the diastereoisomers of [{Os(bpy)$_2$}$_2$(μ-BL)]$^{4+}$ (BL = ppz, 2,3-dpp) was characterized by the appearance of two new bands in the region 3500−10000 cm^{-1} ($\nu_{max} \approx 5000$ and 8300 cm^{-1}), shown in

(95) Richardson, D. E.; Sen, J. P.; Buhr, J. D.; Taube, H. *Inorg. Chem.* **1982**, *21*, 3136−3140.

(96) Brunschwig, B. S.; Sutin, N. *Coord. Chem. Rev.* **1999**, *187*, 233−254.

Table 3. Summary of the Mid-IR and NIR Spectral Data for *meso-* and *rac*-[{Os(bpy)₂}₂(μ-BL)]⁵⁺ in [(*n*-C₄H₉)₄N]PF₆/CH₃CN at −35 °C[a]

	meso		rac	
BL	ν_{max} $\pm10/cm^{-1}$	$(\epsilon/\nu)_{max}$ $\pm0.001/M^{-1}$	ν_{max} $\pm10/cm^{-1}$	$(\epsilon/\nu)_{max}$ $\pm0.001/M^{-1}$
dpb	**2150**	**1.8262**	4820	0.0888
	4920	0.1176	8730	0.5978
	8930	0.5979	12 050	0.3346
	12 220	0.3700		
dpb′	**2060**	**3.699**	4870	0.0630
	4870	0.0848	7045	0.1739
	6810	0.2382	8700	0.6651
	8480	0.7663	11 860	0.6337
	11 600	0.5959		
dpq′	4980	0.1399	4980	0.1079
	8840	0.7750	9190	0.8203
	13 050	0.4783	13 540	0.6290
ppz	**2275**	**2.8906**	5070	0.1126
	5000	0.0930	8400	0.3014
	8340	0.4142	11 180	0.5374
	11 140	0.6074	*sh* 15 800	0.5109
	sh 15 800	0.6082		
2,3-dpp	4950	0.1357	5030	0.1150
	8300	0.5164	8330	0.4519
	11 720	0.4740	11 700	0.4347
	sh 15 970	0.3644	*sh* 16 070	0.3640

[a] The mid-IR spectral data are indicated in bold type.

Figures S9 and S11 (Supporting Information). The more-intense higher-energy band disappeared on removal of the second electron and was assigned as an IVCT transition. This band is asymmetrical and narrower on the lower-energy side, with Gaussian deconvolution revealing the presence of three underlying transitions, as shown in the insets in Figure S9. The first component closely matches the energy, intensity and band-shape of the lower-energy side of the IVCT manifold, while the less-intense higher-energy components give rise to the band asymmetry. The transitions are significantly narrower than those predicted on the basis of the classical two-state theory,[5] which indicates significant electronic communication between the metal centers.

The mixed-valence spectra for the diastereoisomers of [{Os(bpy)₂}₂(μ-dpb′)]⁵⁺ were characterized by two new bands at 4870 and ∼7000 cm⁻¹ (Figures S9 and S11). The more-intense, higher-energy band disappeared on removal of the second electron and was assigned as an IVCT transition. Compared with the asymmetrically shaped IVCT bands at ∼8300 cm⁻¹ in the diastereoisomers of [{Os-(bpy)₂}₂(μ-BL)]⁵⁺ (BL = ppz, 2,3-dpp), the bands at 6810 and 7045 cm⁻¹ in *meso-* and *rac*-[{Os(bpy)₂}₂(μ-dpb′)]⁵⁺, respectively, were fitted by a single Gaussian-shaped component.

meso- and *rac*-[{Os(bpy)₂}₂(μ-BL)]⁵⁺ (BL = dpb, dpq′) exhibited two new bands at ∼5000 and ∼7500 cm⁻¹. The latter was observed as a weak shoulder on the low-energy side of the band in the region 7000−9200 cm⁻¹ and was assigned as an IVCT transition. The band in the region 8700−9200 cm⁻¹ is comprised of two underlying transitions of approximately equal intensity, one of which may also represent an IVCT transition.

The extension of the spectroelectrochemical measurements to the mid-IR region revealed an intense {(ε/ν)_max ≈ 1.8−2.9 M⁻¹} asymmetrically shaped band in the region 2000−

4000 cm⁻¹ for *meso-*[{Os(bpy)₂}₂(μ-BL)]⁵⁺ (BL = dpb, dpb′, ppz), as shown in Figure S9a. The band was comprised of two underlying Gaussian-shaped components for the dpb-bridged complex and three underlying components for the dpb′- and ppz-bridged complexes (Table S7, Supporting Information). The overall bandwidth of the manifold and the separation of the underlying components are largest for the dpb-bridged complex due to the additional redox asymmetry contribution arising from the stereochemically induced structural distortion. The separation of the components of the mid-IR band in the Os systems (ca. 1000 cm⁻¹) is comparable to the splittings expected between the underlying IVCT components for their Ru analogues, whereas they might be expected to be greater for the former due to the larger spin−orbit coupling constant. This argues against the assignment of the mid-IR band as IVCT(1) in the Os systems.

Nature of Delocalization: a Qualitative Picture. Since the present systems appear to lie in the borderline region between the localized and delocalized regimes, qualitative arguments based on delocalized and localized pictures of the nature of the electronic delocalization in these systems are considered below.

Delocalized Model. The Os complexes exhibit extensive delocalization, and the IVCT bands in the mixed-valence species are likely to arise from transitions between bonding and antibonding orbitals within the molecular orbitals manifolds. The intense bands in the mid-IR region are due to IC transitions between spin−orbit states that are split by the coupling of the Os^II.5 centers. For all complexes, the relatively low intensity {(ε/ν)_max ≈ 0.1 M⁻¹} asymmetric bands in the region 5000−6600 cm⁻¹, which are comprised of three underlying Gaussian components (Tables S6 and S7, Supporting Information), are likely to represent spin−orbit transitions in a vibronic progression from the intense transitions in the region 2000−4000 cm⁻¹. The nature of the mid-IR and NIR spectral features for the complexes are strikingly similar to the osmium analogue of the Creutz−Taube ion [{Os(NH₃)₅}₂(μ-pyz)]^{n+} (n = 5, 6), which has been interpreted on the basis of complete electronic delocalization.[97−100] In the present case, the new bands in the NIR region 6600−10000 cm⁻¹, which have been identified as IVCT transitions, appear at higher energies compared with the IVCT bands in their Ru analogues (Table 2).

Localized Model. In the fully oxidized forms of *meso-* and *rac*-[{Os(bpy)₂}₂(μ-BL)]⁶⁺ (BL = dpb′, dpq′, ppz, dpb, 2,3-dpp), IC transitions are evident in the region 4000−5500 cm⁻¹. These transitions occur at approximately the same energies but exhibit higher intensities compared with the IC transitions at 4580 cm⁻¹ (ε_max = 450 M⁻¹ cm⁻¹) and 5090 cm⁻¹ (ε_max = 360 M⁻¹ cm⁻¹) in [Os(bpy)₃]³⁺.[26] The absence of the two dπ → dπ IC transitions in the NIR region for the

(97) Magnuson, R. H.; Lay, P. A.; Taube, H. *J. Am. Chem. Soc.* **1982**, *105*, 5, 2507−2509.
(98) Magnuson, R. H.; Lay, P. A.; Taube, H. *J. Am. Chem. Soc.* **1983**, *105*, 2507−2509.
(99) Lay, P. A.; Magnuson, R. H.; Taube, H. *Inorg. Chem.* **1988**, *27*, 2364−2371.
(100) Dubicki, L.; Ferguson, J.; Krausz, E. R.; Lay, P. A.; Maeder, M.; Taube, H. *J. Phys. Chem.* **1984**, *88*, 3940−3941.

mixed-valence systems [{Os(bpy)$_2$}$_2$(μ-BL)]$^{5+}$ is indicative of the high degree of electronic delocalization in these species.[97−100]

Figure S12 (Supporting Information) shows the mid-IR spectra for *meso*-[{Os(bpy)$_2$}$_2$(μ-ppz)]$^{n+}$ ($n = 5, 6$). By comparison with the mid-IR studies on the +5 and +6 forms of related Class II−III pyz-bridged polypyridyl complexes of osmium such as *cis,cis*-[{Os(bpy)$_2$(Cl)}$_2$(μ-pyz)]$^{3+}$,[101,102] the new vibration at 1625 cm^{-1} in *meso*-[{Os(bpy)$_2$}$_2$(μ-ppz)]$^{5+}$ is analogous to the ν_{8a}(pyz) stretching vibration of pyz.[14] The appearance of this band provides evidence for electronic localization due to a small residual barrier to electron transfer and is consistent with a localized-to-delocalized (Class II−III) classification for the mixed-valence species.

On the basis of this classification, the spectroscopic properties of the mixed-valence states can be interpreted by assuming a small degree of residual localization. The bands in the mid-IR region 2000−4000 cm^{-1} are assigned as IVCT-(1), and the components under the manifold originate from multiple interactions across the bridging ligand between Os-(dπ) orbitals that are highly mixed with π,π^*(BL). While three IVCT and two IC transitions are predicted from a two-site model which includes spin−orbit coupling,[14] the present results suggest that the excited states exhibit multiplicities that are higher than single order. This demonstrates that *at least* a three-site description is necessary to describe the systems; however, a vibronic progression associated with IVCT(1) could also explain the multiple underlying components. The relatively weak bands in the region 5000−6600 cm^{-1} are assigned as d$\pi \rightarrow$ dπ IC transitions and occur in the same range in the +6 state.

The new bands in the NIR region 6600−10 000 cm^{-1} for the mixed-valence species are assigned as IVCT bands. On the basis of the semiquantitative relationships in eq 3,[14] if the transition at ∼8300 cm^{-1} in [{Os(bpy)$_2$}$_2$(μ-BL)]$^{5+}$ (BL = ppz, 2,3-dpp) is assigned as IVCT(2), then IVCT(1) should occur at IVCT(2) − $\Delta E_{so(1)} \approx$ 4000 cm^{-1} ($\Delta E_{so(1)}$ is approximated as the energy of the first IC band in the +6 state from Table S8). However, this predicted position does not correlate with the observed energies of the mid-IR or NIR bands. According to eq 3, the separation between IVCT-(2) and (3) is equated with the separation of the IC states, $\Delta\nu_{IC}$, and IVCT(3) would be assigned as the transition which overlaps IVCT(2) on the higher-energy side.

Clearly, a localized argument is insufficient to rationalize the properties of the dinuclear Os systems. While the mixed-valence species [{Os(bpy)$_2$}$_2$(μ-BL)]$^{5+}$ (BL = dpb, 2,3-dpp) have previously been assigned as localized systems by Brewer and co-workers,[72] it is evident that the full series of complexes in the present study lie at the borderline between the localized-to-delocalized and delocalized regimes.

Stereochemical Effects on the IC Transitions in [{Os-(bpy)$_2$}$_2$(μ-BL)]$^{6+}$. In the +6 state, the trends in the IC bands

(101) Demadis, K. D.; El-Samanody, E.-S.; Coia, G. M.; Meyer, T. J. *J. Am. Chem. Soc.* **1999**, *121*, 535−544.
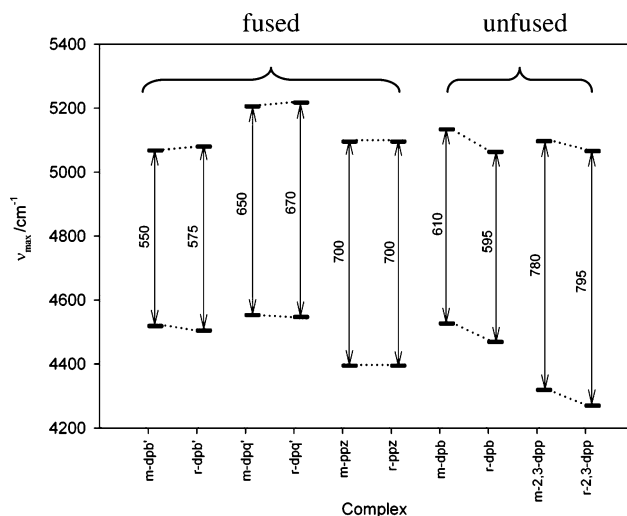(102) Demadis, K. D.; Neyhart, G. A.; Kober, E. M.; White, P. S.; Meyer, T. J. *Inorg. Chem.* **1999**, *38*, 5948−5959.

Figure 4. Schematic diagram of the energies of the IC bands (obtained by spectral deconvolution) for the meso and rac diastereoisomers of [{Os-(bpy)$_2$}$_2$(μ-BL)]$^{6+}$ (BL = dpb′, dpq′, ppz, dpb, 2,3-dpp), abbreviated m-BL or r-BL, respectively.

also provide evidence for stereochemical and structural influences on the dπ(Os) energy levels. Figure 4 provides a schematic illustration of the energies of the IC states, and a summary of the band parameters for the IC transitions is provided in Table S8 (Supporting Information). $\Delta\nu_{IC}$ increases as BL is varied in the order dpb′ < dpb < dpq′ < ppz < 2,3-dpp, and because of structural distortion, this splitting is greater for the diastereoisomers incorporating the unfused bridging ligands dpb and 2,3-dpp compared with their fused analogues dpb′ and ppz. While the IC energies are comparable for both diastereoisomers in the complexes incorporating the fused bridging ligands, the $\Delta\nu_{1/2}$ values for the IC transitions differ significantly between the diastereoisomeric forms of the complexes bridged by dpb and 2,3-dpp. The IC bands occur at higher energies in the meso relative to the rac forms for the complexes due to the larger magnitude of the stereochemically induced redox asymmetry, ΔE_{struct}. These observations are illustrated by the overlays of the IC bands for the full series of complexes in Figure S11 (Supporting Information).

From the trends in the characteristics of the IC bands in the +6 states, three major conclusions may be drawn regarding the contribution of $\Delta E'$ to the IVCT band energy in eq 1. First, since the local site symmetry at each Os center is similar over the series of complexes incorporating the fused bridging ligands, the differences in the energies and splittings of the IC bands must arise from differences in the electronic coupling. Second, the absolute energies of the IC transitions are influenced by stereochemically induced structural distortions, and $\Delta\nu_{IC}$ increases in the presence of such distortions. Third, an increase in $\Delta\nu_{IC}$ in the +6 states of the Os complexes as BL is varied in the order dpb′, dpq′, and ppz is reflected by the broadening of the IVCT bands in their Ru analogues, corresponding to an increase in $\Delta\nu_{IC}$ (Table 2). Since both diastereoisomers of a given Os complex exhibit similar $\Delta\nu_{IC}$ values, the separation of the three underlying components of the IVCT bands in the Ru systems should also be similar for both diastereoisomers of a given

complex. For example, the separation of the IC bands are comparable for both diastereoisomers of [{Os(bpy)$_2$}$_2$(μ-dpb)]$^{6+}$; however, the orbital energies of the IC states are greater for the meso relative to the rac diastereoisomer (Table 3 and Figure 4), which must arise from the larger ΔE_{struct} contribution in the former case. The relatively greater degree of electronic coupling in the rac diastereoisomer is also evidenced by the higher values of $(\epsilon/\nu)_{max}$, M_0, and $|\mu_{12}|$ and the narrower bandwidth compared with the meso form for the analogous Ru system reported in Table 2. Differences in the $\Delta\nu_{1/2}$ values between the diastereoisomers of the Ru systems arise from stereochemically dependent solvent coupling, ion-pairing, and thermochromic effects which have indeed been observed previously for the dinuclear ruthenium complexes.[28–30]

Stark Absorption Spectroscopy. Stark absorption spectra were obtained for the dinuclear complexes meso-[{Ru-(bpy)$_2$}$_2$(μ-BL)]$^{5+}$ (BL = dpb, dpq′) and meso-[{Os(bpy)$_2$}$_2$-(μ-BL)]$^{5+}$ (BL = dpb, dpb′, dpq′, ppz) in n-butyronitrile glass at 77 K and a field strength $\mathbf{F}_{ext}$ of 4.0 MV cm^{-1}. The quantitative Liptay analysis[45] of the Stark response[42,43,46] yielded the dipole moment change ($|\Delta\mu|$), the angle between the transition moment and the dipole moment change (ξ), the difference polarizability ($\Delta\alpha$), and magnitude of the trace of the difference polarizability {Tr($\Delta\alpha$)}. The results for the absorption {$A(\nu)$ vs ν} and Stark absorption {$\Delta A(\nu)$ vs ν} spectra for the dinuclear ruthenium and osmium complexes are presented in Tables 4 and S8 (Supporting Information), respectively. The spectra for meso-[{Ru(bpy)$_2$}$_2$(μ-dpb)]$^{5+}$ and meso-[{Os(bpy)$_2$}$_2$(μ-ppz)]$^{5+}$ are shown in Figures 5 and 6, respectively, where panel a shows the unperturbed absorption spectrum, and panels b and c show the first and second derivatives of the absorption spectrum, respectively. The Stark spectrum and the best fit to the spectrum are shown in panel d. The corresponding spectra for meso-[{Os(bpy)$_2$}$_2$-(μ-BL)]$^{5+}$ (BL = dpq′, dpb′) are shown in Figures S13 and S14 (Supporting Information).

The most notable feature of the Stark signals for the IVCT bands in meso-[{Ru(bpy)$_2$}$_2$(μ-dpb)]$^{5+}$ (Figure 5) and meso-[{Ru(bpy)$_2$}$_2$(μ-dpq′)]$^{5+}$ in the range 3050–12 500 cm^{-1} is the absence of a strong second-derivative component. This is indicative of a minimal dipole moment change, $|\Delta\mu_{12}|$, accompanying the IVCT excitation and a negligible adiabatic charge-transfer distance, r_{12} (eq 7).

$$r_{12} = |\Delta\mu_{12}|/e \qquad (7)$$

The Stark spectrum strongly resembles the negative of the unperturbed (zeroth-derivative) absorption spectrum at energies below the maximum of the overall IVCT manifold, and the low-energy side of the Stark signal was modeled well by a negative zeroth derivative. At energies above the absorption maximum, the Stark spectrum exhibits a slightly positive $\Delta A(\nu)$ component which is indicative of a contribution from the first derivative.

For meso-[{Ru(bpy)$_2$}$_2$(μ-BL)]$^{5+}$ (BL = dpb, dpq′), poor fits were obtained from attempts to reproduce the Stark signal over the entire IVCT manifold as the high-energy side of
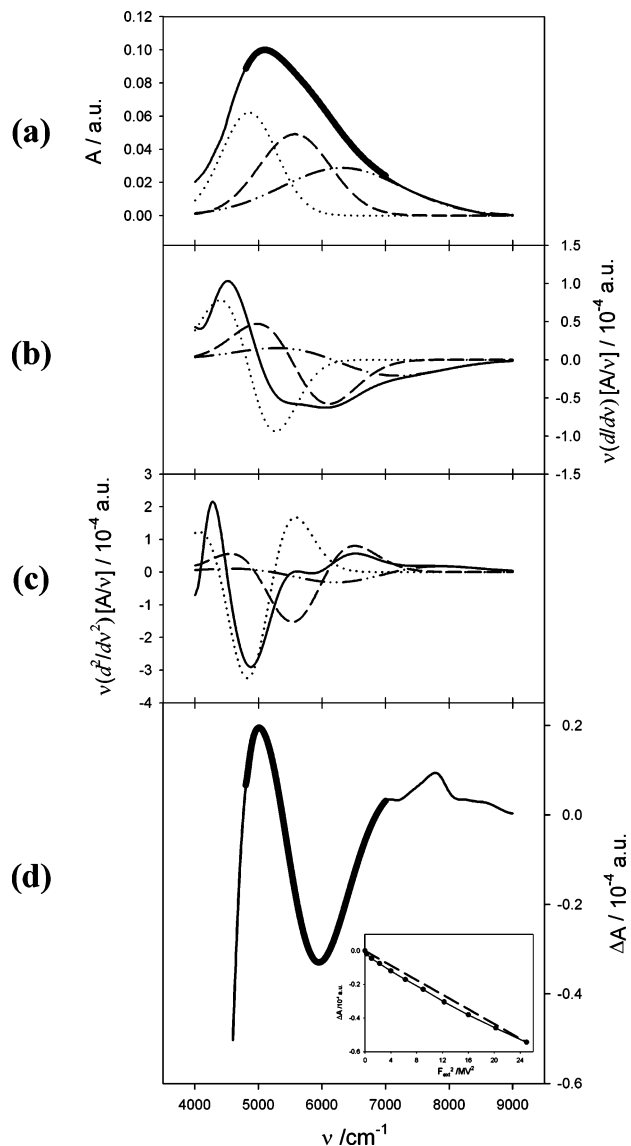

Figure 5. Liptay analysis of the Stark absorption spectrum (A vs ν) for meso-[{Ru(bpy)$_2$}$_2$(μ-dpb)]$^{5+}$ in n-butyronitrile glass at 77 K with a field strength of 4.0 MV cm^{-1}. (a) Unperturbed absorption spectrum with the bands obtained by Gaussian deconvolution and energy weighted first (b) and second (c) derivatives of the absorption spectrum. In each case, the deconvoluted bands are shown as (· · ·), (— · —) and (— — —). (d) Measured (—) and fitted (thick dashed line) Stark signals (ΔA vs ν) at 45°. The inset shows the Stark response at 6500 cm^{-1} as a function of $\mathbf{F}_{ext}^2$ (the predicted ΔA vs $\mathbf{F}_{ext}^2$ dependence is — — —).

the signal behaved in a complicated manner, suggesting multiple underlying bands with different field dependencies. The inset in Figure 5d shows the dependence of $\Delta A(\nu)$ on $\mathbf{F}_{ext}^2$ at 6500 cm^{-1} for meso-[{Ru(bpy)$_2$}$_2$(μ-dpb)]$^{5+}$. While eq 5 assumes a linear variation between these parameters, the deviation from linearity indicates a breakdown of the Liptay equations. The best fits were obtained using three underlying components (previously assigned as spin–orbit components in the ruthenium systems). From Table 4, the results for the parameters obtained from the Liptay analysis of each component show small or negligible dipole moment changes, which are indicative of essentially complete delocalization. In addition to the non-Liptay behavior implied by the nonlinear dependence of $\Delta A(\nu)$ on $\mathbf{F}_{ext}^2$, the magnitudes of the polarizability changes—which are too large to
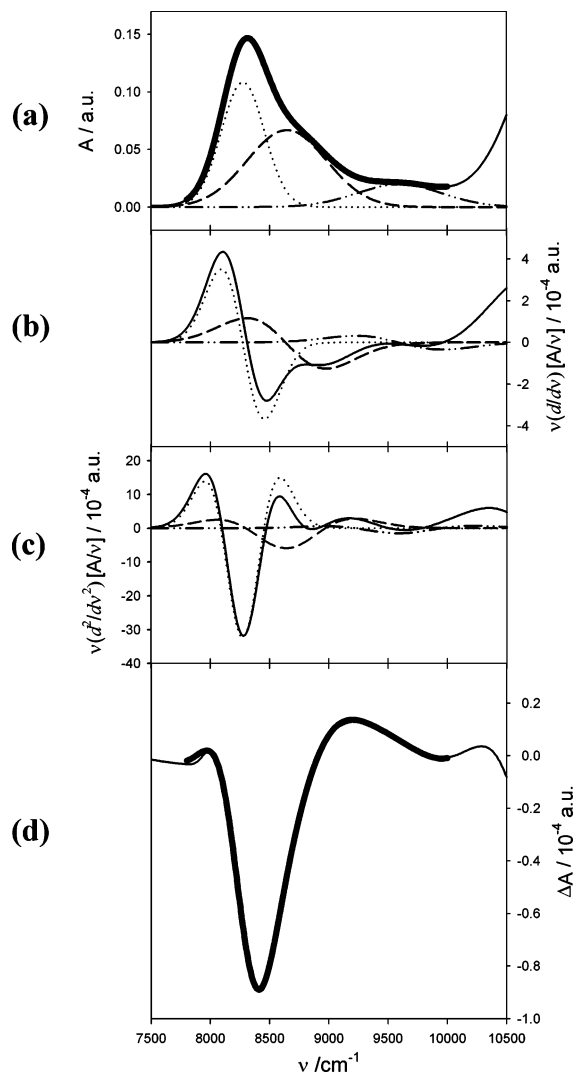
Figure 6. Liptay analysis of the Stark absorption spectrum (*A* vs *ν*) for *meso*-[(Os(bpy)₂)₂(*μ*-ppz)]⁵⁺ in *n*-butyronitrile glass at 77 K with a field strength of 4.0 MV cm⁻¹. (a) Unperturbed absorption spectrum with the bands obtained by Gaussian deconvolution and energy weighted first (b) and second (c) derivatives of the absorption spectrum. In each case, the deconvoluted bands are shown as (· · ·), (− · −) and (− − −). (d) Measured (—) and fitted (thick dashed line) Stark signals (Δ*A* vs *ν*) at 45°.

Table 4. Absorption and Electroabsorption Properties of the IVCT Bands for *meso*-[{Ru(bpy)₂}₂(*μ*-BL)]⁵⁺ (BL = dpb, dpq′) in *n*-butyronitrile Glass at 77 K and a field strength of 4.0 MV cm⁻¹ᵃ

BL	ν_{max} /cm⁻¹	$\Delta\nu_{1/2}$ /cm⁻¹	$|\Delta\mu_{12}|$ /eÅ	$|\Delta\mu_{12}|$ /D	ξ /deg	Tr($\Delta\alpha$) /Å³	$\Delta\alpha$ /Å³
dpb	4810	1030	0.38(2)	1.8(2)	−22	−200	−466
	5515	1330	∼0	∼0	0	657	1300
	6165	2250	∼0	∼0	0	−1080	−577
dpq′	5195	1110	0.32(3)	1.5(2)	0	−796	−1193
	6050	1130	∼0	∼0	17	−8095	−10 530
	6830	1500	∼0	∼0	0	−21 195	−34 510

ᵃ The errors in the observed and calculated parameters (not tabulated) are ±10 cm⁻¹ for ν_{max} and $\Delta\nu_{1/2}$, ±2° for ξ, and ±10 Å³ for Tr($\Delta\alpha$) and $\Delta\alpha$.

be physically meaningful—are also indicative of nonclassical Stark effects. While the values for the polarizability changes may also reflect artifacts arising from decisions regarding the spectral deconvolutions, values of >10³ Å³ were obtained for Tr($\Delta\alpha$) and $\Delta\alpha$ from attempts to fit the entire IVCT manifold by a single set of Liptay parameters. In view of

the non-Liptay behavior, the parameters derived from the analysis (particularly the polarizability parameters) cannot be interpreted quantitatively.[103] The major conclusions which can be drawn from the analyses is the presence of small dipole moment changes for both complexes, which are indicative of a small degree of charge-transfer character, and a borderline localized-to-delocalized or delocalized classification.

The Stark spectra for *meso*-[{Os(bpy)₂}₂(*μ*-BL)]⁵⁺ (BL = dpb, dpb′, dpq′, ppz) were obtained over the range 3850−20 000 cm⁻¹ and were fitted to a combination of multiple Gaussian components. In each case, the relative energies, intensities, and bandwidths for the underlying transitions in the spectra were consistent with those reported in Tables S6 and S7. Due to the errors involved in fitting the Stark spectra for the weak transitions in the NIR region 3850−6000 cm⁻¹ and the significantly convoluted nature of the spectra, Table S9 presents the results for the major absorption bands only. Attempts to fit the IVCT manifolds using a single set of Liptay parameters resulted in significant deviations of the fits at energies above the band maxima, as illustrated in Figure S15 (Supporting Information) for the *meso*-[{Os-(bpy)}₂(*μ*-ppz)]⁵⁺.

Figure 6a shows the IVCT band and spectral components in the region 6000−10 000 cm⁻¹ for *meso*-[{Os(bpy)₂}₂(*μ*-ppz)]⁵⁺, and Figure 6b and c shows the first and second derivatives of the IVCT band. The IVCT Stark signal (Figure 6d) was modeled in terms of a negative zeroth derivative on the low-energy side and a positive $\Delta A(\nu)$ contribution on the higher-energy side. The negligible dipole moment changes reported in Table S9 are consistent with the previous classification of the system at the borderline between the localized-to-delocalized and delocalized regimes. Interestingly, the absorption and Stark absorption line-shapes are reminiscent of those observed for the IVCT band at 6410 cm⁻¹ (in D₂O) in the Creutz−Taube ion,[104] where the change in dipole moment of 0.7 ± 0.1 D was significantly smaller than the calculated value of 32.7 D for unit electron transfer across the 6.9 Å pyz bridge (1:1 glycerol/water at 77 K; 1 MV cm⁻¹ field strength). As shown in Table S8, the small magnitudes of the dipole moment changes are a characteristic feature of the full series of *meso*-[{Os(bpy)}₂(*μ*-BL)]⁵⁺ complexes and support significant delocalization in all cases. This contradicts the previous Class II assignment for the complexes [{Os(bpy)₂}₂(*μ*-BL)]⁵⁺ (BL = dpb, 2,3-dpp) by Brewer and co-workers,[72,73] which was based on a classical two-state analysis of the NIR spectra.

Conclusions

The mixed-valence systems [{Os(bpy)₂}₂(*μ*-BL)]⁵⁺ (BL = dpb′, dpq′, ppz, dpb, 2,3-dpp) are characterized by multiple IVCT and IC bands in the mid-IR and NIR regions, and the lowest energy IVCT band occurs in the mid-IR region 2000−4000 cm⁻¹. Differences in the relative energies of the IC

(103) Dinolfo, P. H.; Williams, R. D.; Hupp, J. T. **2005**, submitted for publication.
(104) Oh, D. H.; Boxer, S. G. *J. Am. Chem. Soc.* **1990**, *112*, 8161−8162.

transitions in the NIR region for the fully oxidized (+6) states demonstrate that stereochemical effects lead to fundamental changes in the energy levels of the metal-based $d\pi$ orbitals which are split by spin−orbit coupling and ligand-field asymmetry. While the separation between the IC bands is relatively invariant for the diastereoisomeric forms of each species, their absolute energies are lower for the rac relative to the meso forms of the complexes incorporating the unfused bridging ligands dpb and 2,3-dpp. The results have important implications for the analysis of the underlying spin−orbit coupling transitions in the analogous dinuclear ruthenium systems. For the series of complexes incorporating the fused bridging ligands, the increase in the separation between the IC bands as BL is varied through the series dpb′, dpq′, and ppz reflects the increase in the degree of electronic coupling. The effect is attributed to the increase in the separation of the three underlying components of the bands.

Stark effect measurements on the meso diastereoisomers of [{Ru(bpy)$_2$}$_2$(μ-BL)]$^{5+}$ (BL = dpq′, dpb) and [{Os(bpy)$_2$}$_2$(μ-BL)]$^{5+}$ (BL = dpb′, dpq′, ppz, dpb) reveal that negligible dipole moment changes accompany IVCT excitation. This provides independent support for the classification of the dinuclear ruthenium and osmium complexes as delocalized systems. Since the mid-IR spectra suggest the presence of residual localization, the systems fall in the borderline region between the localized and delocalized regimes, with the osmium systems exhibiting a higher extent of electronic coupling than their ruthenium counterparts.

The series of complexes [{Ru(bpy)$_2$}$_2$(μ-BL)]$^{4+}$ based on the bridging ligands shown in Figure 2 have been investigated extensively over the past two decades as the basis of novel molecular materials capable of performing useful light- and redox-induced functions.[31−35] While these studies were performed without regard for the inherent stereochemistry of the systems, the present work demonstrates that stereochemical influences provide a significant contribution to the barrier to intramolecular electron transfer and are indeed manifested in the electrochemical, spectral, and IVCT properties of the systems. The realization that metal−metal interactions in dinuclear polypyridyl complexes can be modified by the variation of their stereochemical properties has significant consequences for controlling such interactions in higher-nuclearity polymetallic assemblies.

Supporting Information Available: Tables of crystal data and structure refinement parameters; electrochemical and UV/vis/NIR data for dinuclear Os and Ru complexes; parameters from deconvolution of IVCT spectra; mid-IR spectral data; energies of IC transitions for Os absorption and electroabsorption properties of NIR bands; ^{1}H NMR data and assignments; ORTEP plots with atom numbering for meso-[{Os(bpy)$_2$}$_2$(μ-dpb)]$^{4+}$ and meso-[{Os(bpy)$_2$}$_2$-(μ-dpq′)]$^{4+}$; differential mid-IR spectra; overlays of NIR spectra; and Liptay analyses of Stark absorption spectra. This material is available free of charge via the Internet at http://pubs.acs.org.

IC051841F